Kerem Pekkan
Assistant Professor
Department of Biomedical Engineering,
Carnegie Mellon University,
2100 Doherty Hall,
Pittsburgh, PA 15213-3890
e-mail: kpekkan@andrew.cmu.edu

Onur Dur
Department of Biomedical Engineering,
Carnegie Mellon University,
2100 Doherty Hall,
Pittsburgh, PA 15213-3890

Kartik Sundareswaran
Cardiovascular Fluid Mechanics Laboratory,
Wallace H. Coulter Department of Biomedical Engineering,
Georgia Institute of Technology,
315 Ferst Drive,
Atlanta, GA 30332-0535

Kirk Kanter
Pediatric Cardiothoracic Surgery,
Emory University School of Medicine,
1440 Clifton Road,
Atlanta, GA 30322

Mark Fogel
Children's Hospital of Philadelphia,
34th Street,
Civic Center Boulevard,
Philadelphia, PA 19104

Ajit Yoganathan
Cardiovascular Fluid Mechanics Laboratory,
Wallace H. Coulter Department of Biomedical Engineering,
Georgia Institute of Technology,
315 Ferst Drive,
Atlanta, GA 30332-0535A

Akif Ündar
Department of Pediatrics,
Surgery and Bioengineering,
Penn State College of Medicine,
Hershey, PA 17033

Neonatal Aortic Arch Hemodynamics and Perfusion During Cardiopulmonary Bypass

The objective of this study is to quantify the detailed three-dimensional (3D) pulsatile hemodynamics, mechanical loading, and perfusion characteristics of a patient-specific neonatal aortic arch during cardiopulmonary bypass (CPB). The 3D cardiac magnetic resonance imaging (MRI) reconstruction of a pediatric patient with a normal aortic arch is modified based on clinical literature to represent the neonatal morphology and flow conditions. The anatomical dimensions are verified from several literature sources. The CPB is created virtually in the computer by clamping the ascending aorta and inserting the computer-aided design model of the 10 Fr tapered generic cannula. Pulsatile (130 bpm) 3D blood flow velocities and pressures are computed using the commercial computational fluid dynamics (CFD) software. Second order accurate CFD settings are validated against particle image velocimetry experiments in an earlier study with a complex cardiovascular unsteady benchmark. CFD results in this manuscript are further compared with the in vivo physiological CPB pressure waveforms and demonstrated excellent agreement. Cannula inlet flow waveforms are measured from in vivo PC-MRI and 3 kg piglet neonatal animal model physiological experiments, distributed equally between the head-neck vessels and the descending aorta. Neonatal 3D aortic hemodynamics is also compared with that of the pediatric and fetal aortic stages. Detailed 3D flow fields, blood damage, wall shear stress (WSS), pressure drop, perfusion, and hemodynamic parameters describing the pulsatile energetics are calculated for both the physiological neonatal aorta and for the CPB aorta assembly. The primary flow structure is the high-speed canulla jet flow ($\sim$3.0 m/s at peak flow), which eventually stagnates at the anterior aortic arch wall and low velocity flow in the cross-clamp pouch. These structures contributed to the reduced flow pulsatility (85%), increased WSS (50%), power loss (28%), and blood damage (288%), compared with normal neonatal aortic physiology. These drastic hemodynamic differences and associated intense biophysical loading of the pathological CPB configuration necessitate urgent bioengineering improvements—in hardware design, perfusion flow waveform, and configuration. This study serves to document the baseline condition, while the methodology presented can be utilized in preliminary CPB cannula design and in optimization studies reducing animal experiments. Coupled to a lumped-parameter model the 3D hemodynamic characteristics will aid the surgical decision making process of the perfusion strategies in complex congenital heart surgeries. [DOI: 10.1115/1.2978988]

1 Introduction

Staged palliation of complex congenital heart defects requires open heart surgeries very early in life. Radical surgical reconstructions of the circulation system result in drastic differences in pre- and postoperative systemic-to-pulmonary flow (Q_p/Q_s) and cardiac loading, which can be realized through the increased physiological plasticity of the neonatal patient. Prolonged cardiopulmonary bypass (CPB), Fig. 1, is usually required during these surgeries affecting 20,000 children annually. There are well acknowledged deterious effects of standard CPB techniques on neonates [1], including higher inflammation risk, premature Circle of Willis [2], and unbalanced nonphysiological organ perfusion [3,4], resulting in temporary or permanent brain damage in up to 25% of patients. Biomechanical design of improved neonatal CPB circuit components, which is challenged by complex pulsatile and cavitating flows, has to be customized for the patient-specific anatomy and physiology. Geometrically scale-down versions of established adult scale designs have historically demonstrated poor outcome especially in blood damage indices. Most importantly, neonatal cardiac output requirement remains relatively high, which challenges the successful biomechanical design of small diameter pediatric cannulas resulting in high blood trauma due to pulsatile jetlike flow regimes. A validated computational fluid dynamics (CFD) analysis methodology will be instrumental in achieving optimal hemodynamic performance and eventually will bring the poor neonatal CPB outcome close to the adult CPB values.

Pulsatile perfusion systems [5–9], offering several beneficial effects [6,10–13], have been proposed and studied extensively to

Contributed by the Bioengineering Division of ASME for publication in the JOURNAL OF BIOMECHANICAL ENGINEERING. Manuscript received July 13, 2007; final manuscript received April 21, 2008; published online October 15, 2008. Review conducted by B. Barry Lieber.

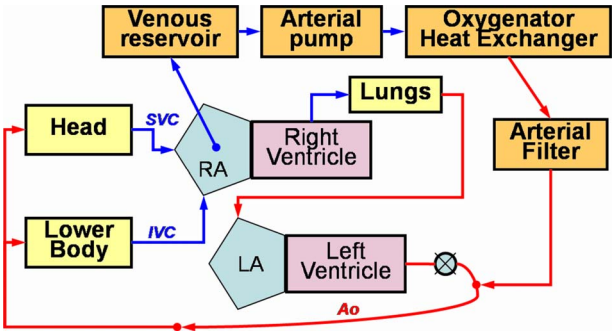

Fig. 1 A schematic of the cardiopulmonary bypass (CPB) circuit. CPB procedures are used extensively during cardiac surgery to withdraw venous blood from the right atrium and pump it through an oxygenator, and then return the oxygenated blood to the patient through the ascending thoracic aorta, bypassing the heart and the lungs. During CPB, the heart is usually arrested and the cardiac surgeon performs the operation on the motionless heart. A cannula is inserted into the patient's right atrium to drain venous return. The venous blood is fed into the venous reservoir by gravity. The blood is pumped through the membrane oxygenator and an arterial filter removes any air bubbles and blood emboli. The blood is then returned into the aorta distal to a cross-clamp (LA: left atrium).

address some of the challenges of neonatal cardiac assist. Rigorous quantitative parameters (energy equivalent pressure and surplus hemodynamic energy) have been defined to compare and evaluate the pulsatile performance of CPB components on a standard basis [14,15]. During CPB, the quality of the artificially produced pulsatile waveform and pulsatile energy cascade is dependent on the pump, membrane oxygenator [16], aortic cannula, and patient-specific vascular compliance [17]. Likewise cannula tip and aortic arch anatomy influence the pulsatile waveforms conducted to the upstream head-neck vessels and descending aorta. Hemodynamics, pulsatile energy loss, and the distribution of the remaining pulsatile energy and cardiac output to various organ compartments [18] through the aortic arch junction are therefore ultimately important. Quantitative evaluation of the CPB hemodynamics has gained even further clinical interest as any improvement in cerebral perfusion can be monitored real-time at the operating room through the transcranial Doppler ultrasound [19] and spatially resolved near infrared spectroscopy, which are emerging as standard diagnostic tools in addition to the traditional electroencephalography and electrocardiography (ECG) monitoring [20]. However, these measurements and earlier physiological investigations in animal models provide only the global perfusion and lumped pulsatile performance peripheral to the aortic junction [21]. Detailed understanding of neonatal aortic arch hemodynamics and characteristic distribution of pulsatile energy to each arterial vessel is essential to achieving improved pediatric CPB cannula designs and optimal neonatal perfusion strategies.

Hemodynamic studies that investigate the effects of cannula orientation are limited to ventricle-assist devices with idealized geometries [22,23], catheterization [24], and venous cannulation [25]; exclusively in adult applications neglecting the neonatal state. Andersen et al. [26] analyzed in vitro hemodynamics of six different 22 Fr adult CPB cannulas and proposed a novel diffuser tip prototype with significantly reduced pressure drop and turbulent stress. Experimental in vitro studies either ignored the intravascular cannula tip protrusion [27] or the exact aortic cross-clamp anatomy as a first approximation. Sophisticated CFD analysis techniques are also employed but with idealized aortic arch geometries and usually without including the head-neck branches [23]. While these studies provide significant information on blood damage and wall shear stress loading, the pulsatile performance and its distribution to the arterial system have not been modeled. In this study we are able to reconstruct the complete generic CFD model of the neonatal CPB cannulation based on a real pediatric patient-specific aorta morphology through the recent advances in patient-specific surgical planning paradigms and the virtual surgery modeling experience [28–30].

Studied by the pioneer investigators, hemodynamics of the *normal adult-scale* aorta is a classical topic of cardiovascular fluid mechanics [31–33]. In recent literature, wall shear stress and 3D effects have been presented in idealized aortic arch models with neglected head-neck branches at relatively low nonphysiological Reynolds numbers [34]. The effects of realistic inflow boundary conditions, such as the left ventricle pumping action, are observed to produce minor effects on helical flow structures and influenced wall shear stress distributions only in the ascending aorta region [35]. Again with neglected head-neck vessels, Morris et al. [36] presented the hemodynamic characteristics of an adult aortic arch in a patient-specific study that explored the effects of 3D reconstruction from computed tomography (CT) data. An unsteady pressure drop of ~1 kPa is correctly predicted in a combined CFD/MRI patient-specific descending aorta study [37]. Likewise, the MRI data that are reconstructed throughout the cardiac cycle enabled CFD simulations with specified vessel wall motion where aortic valve downstream velocity profiles are studied in a segment of ascending aorta [38] as well as coronary inflow with a rotary aortic root [39,40]. Utilizing a Chimera (overset) mesh allows practical inclusion of head-neck vessels in structured grid CFD models of the aorta [41] showing higher WSS values at the roots of these vessels. While these studies provided important information on the biofluid dynamics of a normal aortic arch, the anatomical size, unsteadiness, and inflow conditions influence the aortic hemodynamics considerably. This is illustrated in the recent studies on mouse aortas governed by lower peak Reynolds and Womersley numbers (~250 and ~2) where significantly higher wall shear stresses are reported [42,43] compared with the human aortic arch, where low and oscillatory WSSs are significantly correlated with spatial protein expressions [43]. Similarly the neonatal aortic arch is a critical physiological time point specifically for congenital surgical planning and deserves a detailed hemodynamic investigation as the left ventricle aortic flow rate doubles during fetal to neonatal transition with the closure of the ductus arteriosus [44]. While this study focuses on the aortic arch flow fields, several pulsatile patient-specific CFD studies have also been performed on thoracic aneurysms [45–49].

The objective of this study is to develop a second-order accurate transient CFD model of the neonatal aortic arch and virtually simulate the pathological condition of CPB cannulation hemodynamics. Cannula and aortic arch are integrated during CPB and are analyzed as an assembly. CFD results are compared with the in vivo measurements. The present manuscript is intended to document the baseline hemodynamics and performance that are typically achieved with a generic neonatal CPB cannula configuration. Further improved configurations and optimized cannula designs could be studied with the presented model. In this manuscript CPB hemodynamic parameters are also compared with the corresponding patient-specific neonatal and pediatric normal aortic flow fields.

2 Methods

2.1 Patient-Specific 3D Neonatal Aorta Morphology. Accurate study of the neonatal CPB hemodynamics requires patient-specific aortic morphology. In this study a three-dimensional (3D) aortic arch reconstruction from cardiac magnetic resonance imaging (MRI) of a pediatric patient (age: 10 years, body surface area: 1.32 m^2) with a normal aortic morphology (NIH-Georgia Tech Fontan Anatomy Database ID: CHOP30) was scaled down to represent a neonatal aortic arch with a body surface area (BSA) of 0.1872 m^2. This BSA also corresponds to the well established 3 kg piglet neonatal animal model [50] where in vivo physiological measurements during CPB were available for validation from the

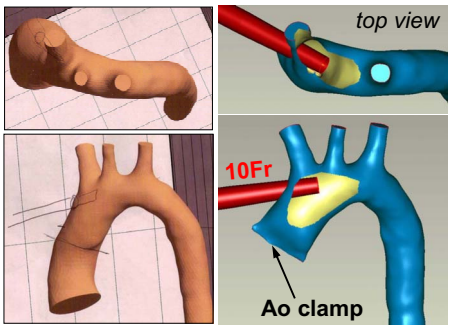

Fig. 2 (Left) Surgeon sketches of the CPB assembly, including the aortic cross-clamp location, are prepared by pediatric surgeon; top and bottom views. (Right) CPB cannulation (tapered 10 Fr) is created "virtually" on the computer based on the patient-specific "surgical planning" modeling protocols.

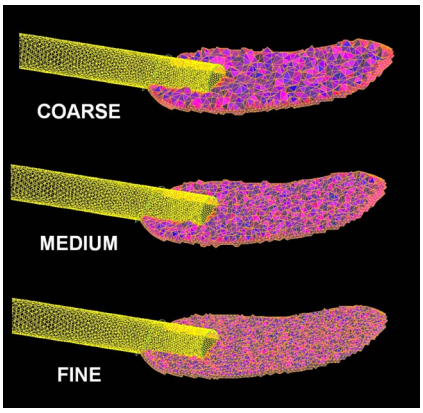

Fig. 3 Close-up view of the tetrahedral grids at the cannula tip region for the CPB Ao model. The grids are shown on an axial plane that goes through the aortic arch.

earlier studies [17,21]. The scale-down factor for linear dimensions was calculated to be 0.4324 [51,52]. The primary dimensions of both models were further verified by clinical measurements from healthy neonatal [53] and pediatric [54] subjects. 3D anatomical reconstruction techniques developed for complex congenital vascular anatomies have been described earlier [55–58] and were applied to the present problem with minor changes.

2.2 PC-MRI Acquisition and Analysis. This study utilized a Siemens 1.5 T whole body MRI scanner for the acquisition of patient-specific boundary conditions. Retrospectively triggered, through-plane, phase-encoded velocity mapping was performed on a plane perpendicular to the flow in the ascending aorta positioned approximately 2 mm above the aortic valve. The velocity encoding used was ± 150 cm/s. The effective repetition time was 20 ms, which yielded 30 cardiac phases, the echo time was 2.5 ms, and the image matrix size was 128×256 pixels. The field of view was about 30 mm and a rectangular field of view was used. The slice thickness was 5 mm. The ascending aorta was then semi-automatically segmented using a gradient based active contour scheme and flow was quantified throughout the cardiac cycle.

2.3 Virtual CPB Cannulation. Three-dimensional surgeon sketches describing the pediatric CPB cannulation using a 10 Fr cannula are prepared for the 3D aortic reconstruction, Fig. 2. Using these sketches the CPB is created virtually in the computer by cross-clamping the ascending aorta [59] and inserting the computer-aided design model of the 10 Fr tapered generic cannula (OD: 3.3 mm, ID: 2.46 mm). Cannula and aortic arch are oriented with respect to each other to simulate a typical standard pediatric CPB configuration, Fig. 2. Generic cannula dimensions are selected to be similar to a DLP75010 (measured as OD: 3.23 mm and ID: 2.41 mm) aortic cannula since in vivo physiological measurements are available.

This configuration now corresponds to a complete generic model of the neonatal CPB cannulation based on a real patient-specific aorta morphology made possible through the recent advances in patient-specific surgical planning technologies [60] and our virtual surgery experience [28–30].

2.4 Computational Fluid Dynamics

2.4.1 Grid Generation. High-quality tetrahedral grids are generated using GAMBIT (Fluent Inc., Lebanon, NH) with three different refinement levels for both neonatal aortic arch and CPB configuration models, Fig. 3. The parameters used in grid generation are summarized in Table 1. To achieve good convergence in unsteady CFD simulations strict mesh quality checks are performed.

2.4.2 Solver Parameters. The CFD model is based on a recent experimentally validated second-order accurate incompressible model that is specially developed to resolve high-frequency time-dependent flow instabilities that are encountered in complex cardiovascular anatomies [61]. The simulations are performed using FLUENT version 6.3.26, with blood properties taken consistent with previous numerical studies ($\rho = 1060$ kg/m^3, $\mu = 3.71 \times 10^{-3}$ Pa s). Flow is incompressible and assumed Newtonian. The unsteady implicit pressure based solver with second-order implicit time advancement scheme, which has broader stability and faster convergence characteristics for unsteady incompressible flows, is chosen. The continuity equation and the linearized momentum equations are solved sequentially using a segregated algorithm. The pressure-velocity coupling algorithm is set as pressure-implicit with splitting of operators (PISO) with skewness correction in order to improve the convergence in transient calculations in close vicinity of distorted cells. Since the entire flow domain was meshed with tetrahedral elements, second-order discretization of pressure and momentum terms is necessary to eliminate numerical diffusion in calculations. Therefore, second-order upwind scheme is applied to discretize the convective terms in momentum equations. The curved nature of anatomic geometry yielded a considerable swirl rate, which is taken into account by setting the pressure staggering option (PRESTO) scheme as the pressure interpolation method. Second-order accurate discretization of pressure terms yielded prominently better results for the cannula model. The convergence is achieved by obtaining a preliminary solution with first-order discretization methods and then setting this as an initial condition to advance second-order accuracy. In addition, the derivatives are evaluated by the node based gradient method, which offers a second-order spatial accuracy for the unstructured computational grid. The simulations are continued for three cycles, which is found to be sufficient for the start-up effects to disappear and the flow to become periodic.

The convergence is monitored by means of the velocity monitors assigned at the designated points of the flow domain (i.e., velocity inlet, aortic arch, and descending aorta). In addition, the residual of continuity equation is reduced to at least 10^{-6} at all time steps. Simulations are performed using both Windows and Linux systems operating on a 3.2 GHz, 32 bit Intel Pentium 4

Table 1 Mesh numbers and parameters used for the normal neonatal model (normal Ao) and for the aorta-cannula CPB assembly (CPB Ao)

Model	Coarse	Medium	Fine
Normal Ao	158,565	329,580	598
CPB Ao	132,290	246,547	436,207
Mesh density	1.35	1.0	0.8

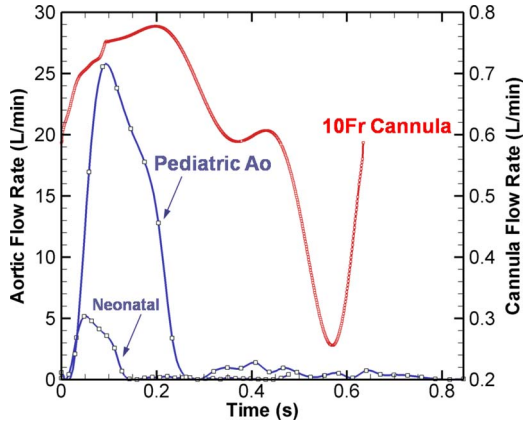

Fig. 4 Inlet flow waveforms specified in neonatal aorta, 10 year old pediatric aorta, and neonatal cardiopulmonary bypass cannula

processor with 3.0 GB RAM with the "Hyper-Threading" option and eight parallel Itanium2 Montvale 9130M dual-core processors with 8.0 GB RAM shared memory respectively. Computations took approximately 40 h (18 h in high-performance parallel setting) to simulate two converged cycles with a period of 0.635 s.

2.4.3 Neonatal Animal Model and Boundary Conditions. The total cardiac output is specified to be 0.894 L/min for the neonatal healthy patient based on the 0.1872 m^2 BSA [62]. A normal newborn heart rate of 130 bpm is also used in this model. Based on these two values, the actual in vivo aortic flow waveforms (3.49 L/min and 50.68 bpm) of the 10 year old patient-specific aortic morphology, acquired through PC-MRI measurements, are scaled and used as boundary conditions for the CFD simulations, Fig. 4. For robust functioning of boundary conditions the small in vivo backflow is neglected.

For the CPB model with a 10 Fr aortic bypass cannulla, the in vivo inlet flow waveforms measured from an earlier 3 kg piglet animal experiment [17,21] with DLP75010 cannula are used, Fig. 4. During this experiment the pump flow rate was fixed delivering an average of 0.6 L/min at a frequency of ~94 bpm. These velocity inlet boundary conditions are assigned to the three-diameter extended inlet surfaces of the ascending aorta or cannula as a plug-flow by means of a user defined function (UDF). The assumption of a flat velocity profile at the aortic inlet has been confirmed from in vivo measurements (see Ref. [36] for a good review).

Mass flow-split boundary conditions of FLUENT, which interpolate velocity profile from the interior of the domain and scale based on the specified flow-split, have been explored in detail in a previous communication [61]. This study showed that the flow-split boundary condition, which is very practical for cardiovascular flows with multiple outlets, performs equally well as standard velocity or pressure outflow boundary conditions (see also the recent Ref. [63]). For both models, the total cardiac output is distributed between the head-neck vessels and the descending aorta (DAo) with the two ratios ranging from 40/60 (corresponding to the in vivo patient-specific PC-MRI) to 50/50. An equal (50/50) total cardiac output share between the head-neck and the DAo is a valid assumption for a normal newborn flow-split [64]. Flow-split during the actual CPB varies considerably [65] but it is likely to be maintained between these two flow-splits. All outlets are extended nine diameters normal to the vessel cross section. The flow-split weighting coefficients of head-neck vessels are calculated proportional to the area of each artery as 0.2, 0.08, and 0.12 for the innominate, left common carotid, and left subclavian arteries (LSAs), respectively (for the 40/60 split case). The vessel surfaces are treated as rigid and impermeable walls.

2.5 Hemodynamic Performance Parameters. The main focus of the present study is to characterize the pulsatile hemodynamic performance and the detailed pulsatile energy characteristics of neonatal aortic arch both at normal and during CPB. Quantitative parameters calculated from CFD solutions include energy equivalent pressure (EEP) (mm Hg), surplus hemodynamic energy (SHE) (ergs/cm^3), pulsatile energy dissipation (P_{loss}, mW), and dissipation function (Φ, mW/m^3).

$$\text{EEP} = \int Q \cdot P dt / \int Q dt \tag{1}$$

$$\text{SHE} = 1332 \cdot \left(\text{EEP} - \int P dt / T \right) \tag{2}$$

$$P_{\text{loss}} = \sum\nolimits_{\text{inlet}} P \cdot Q - \sum_{\text{outlets}} P \cdot Q \tag{3}$$

$$\Phi = 2\mu \left[\left(\frac{\partial u}{\partial x} \right)^2 + \left(\frac{\partial v}{\partial y} \right)^2 + \left(\frac{\partial w}{\partial z} \right)^2 \right] + \left(\frac{\partial u}{\partial y} + \frac{\partial v}{\partial x} \right)^2 + \left(\frac{\partial w}{\partial y} + \frac{\partial v}{\partial z} \right)^2 + \left(\frac{\partial w}{\partial x} + \frac{\partial u}{\partial z} \right)^2 \tag{4}$$

In the above equations, the average flow rate (Q) and total pressure (P) values at the arterial branches are obtained through in vitro experiments or computational simulations. The three velocity components are denoted by (u,v,w), the spatial coordinates are denoted by (x,y,z), and the cardiac cycle is denoted by (T) in seconds.

While the former two parameters, Eqs. (1) and (2), have been utilized extensively in literature [14,15,66] to quantify the pulsatility performance, the later power loss parameter [57,67,68], Eq. (3), is presented in this manuscript as an index of temporal pulsatile energy loss. SHE represents the extra hemodynamic energy in blood flow available due to the pulsatile pressure and flow waveforms over the integrated mean pressure and mean flow rate. For cannula tip design purposes, the spatial distribution of the dissipation function, Eq. (4), within the aortic junction will highlight the exact locations and time-points of energy losses and therefore will be a useful parameter for targeted cannula design and automated optimization studies.

The 3D CFD results provide not only the global systemic post-cannula pulsatility performance, which was employed and presented in all previous studies, but also the *distribution* of pulsatility to the main organ compartments through the peripheral arterial vessels. Pulsatile energies delivered to the descending aorta, innominate artery, left common carotid, and left subclavian artery are presented in Sec. 3.

In addition to the pulsatile performance parameters and flow structures, blood damages in normal neonatal and CPB configurations are estimated through wall shear stress values (peak and average) and standard stress and residence-time hemolysis models [69], in which the blood damage fraction is given by

$$D_{GW} = (3.62e^{-7}) \tau^{2.416} \cdot t^{0.785} \tag{5}$$

While sophisticated blood damage models that are integral to the CFD studies are highly acknowledged and available in literature [70–73], our objective is only to demonstrate and quantify the relative differences in blood damage in normal and pathological CPB configurations.

3 Results

3.1 CFD Model Verification and Validation. The normal neonatal and the CPB aorta model CFD simulations are performed with three increasing mesh sizes for grid verification study. Both models demonstrated good grid convergence and conclusions are similar. Typical changes between coarse-to-medium and medium-

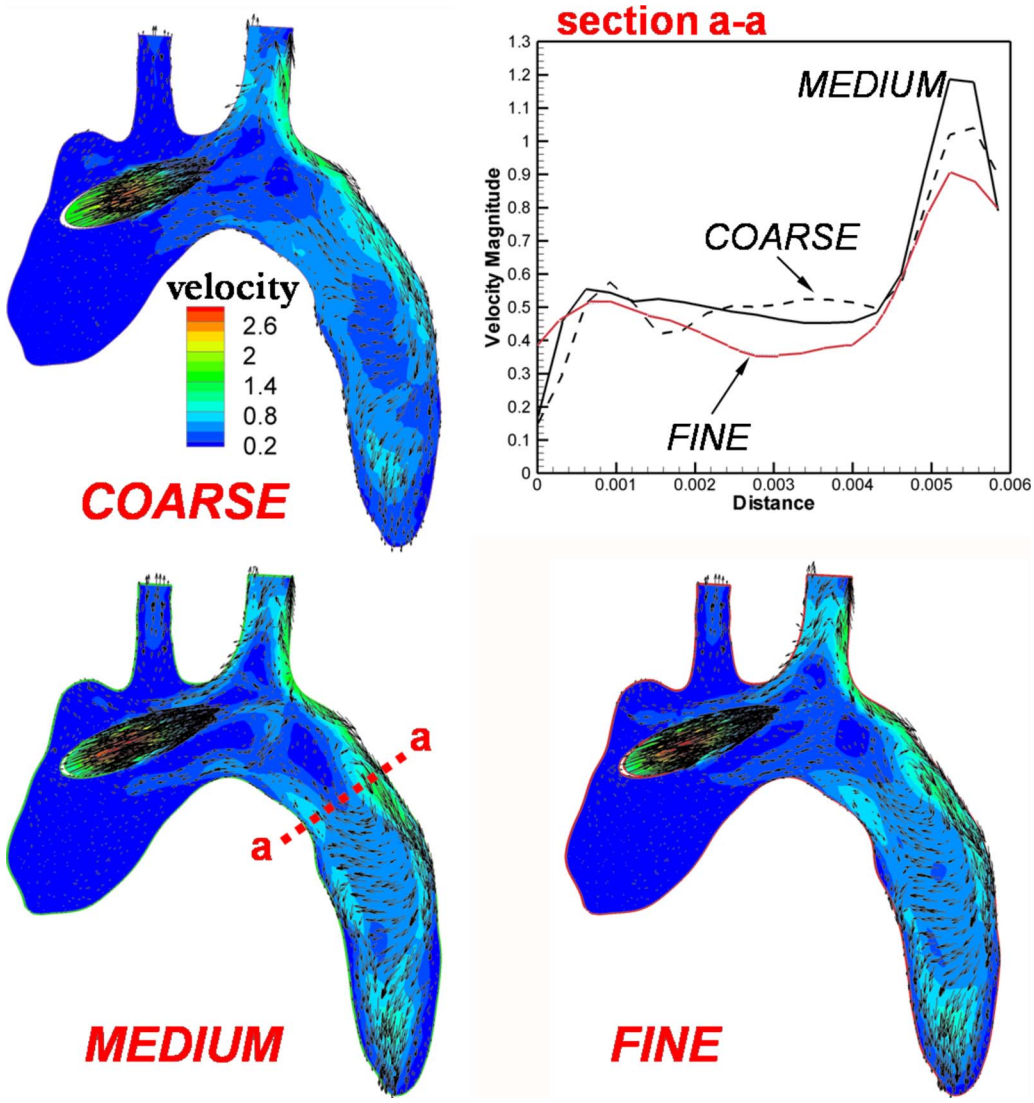

Fig. 5 Comparisons of flow profiles for grid verification study. Velocity magnitudes (m/s) and vectors are plotted along the midsection of the aortic arch. The top right corner shows the detailed comparison of velocity profiles along section a-a. CPB cannula model with 60/40 DAo/head-neck flow-split at t=0.475 s (see Fig. 3).

to-fine grids are plotted for a fixed region in the aortic arch, in the CPB neonatal aorta model, Fig. 5. Velocity profiles are found to be very similar for medium and fine grids. In terms of grid verification, the aorta model with CPB is found to be a more challenging configuration compared with the normal neonatal aorta model and therefore is reported in this manuscript.

For the CPB model CFD results are also compared with the in vivo physiological measurements of a neonatal 3 kg CPB piglet model [17,21]. Both the calculated precannula pressure drop and postcannula arterial pressure waveforms are similar in morphology to the experimental measurements at all grid sizes, Fig. 6. We estimate the postcannula arterial static pressure as the vessel area weighted average pressure of all arterial outlets. In the CFD model this quantity is also very close to the descending aorta pressure waveform. Therefore, both the fine and medium grid neonatal CPB models predicted the in vivo unsteady pressure drop with acceptable accuracy. For medium grid computations the cardiac averaged bias errors are 5.1% and 7.4% for pre- and postcannula pressure waveforms. Inlet precannula pressure peaks are predicted to be lower in the CFD results compared with the in vivo measurements (average of 17.2% difference). These results imply that the medium grid results can be used for unsteady performance predictions and comparative design evaluation. All plotted pressure drops in Fig. 6 are for the 40/60 head-neck to DAo flow-split ratio, the pressure waveform morphology for the 50/50 case was closely similar to the 40/60 split, and the calculated pressure drop is maximum 2.0% lower than the 40/60 split case.

For the numerical time-step used in this study (0.001 s) there were no phase differences in the solutions obtained with different grid sizes as shown in Fig. 6.

3.2 Flow Structures (Neonatal Versus Neonatal With CPB Cannula). In general, the neonatal aortic flow fields are observed to be highly uniform throughout the cardiac cycle. Only during mid-deceleration, flow starts to swirl and separate from the inferior wall of the aortic arch. This regime transforms into short residence-time unstable swirling structures during end-systole due to flow deceleration. These structures are illustrated in Fig. 7(*a*) for different time-points in the cardiac cycle. As expected, introduction of the aortic cannula altered the uniform flow state of the normal neonatal arch dramatically and several swirling complex flow regions are introduced for the entire cardiac cycle as presented in Fig. 7(*a*). This novel flow field experiences a competition between the decelerating cannula jet flow and the outflow

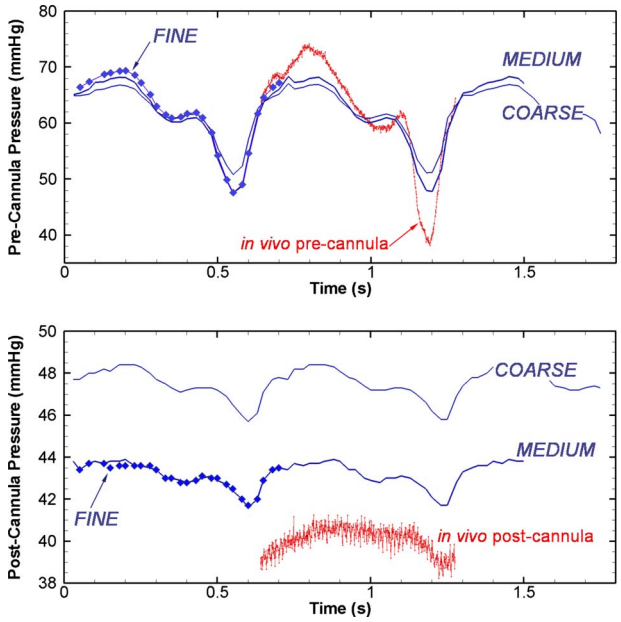

Fig. 6 Comparisons of the calculated pressure waveforms with in vivo physiological measurements for three grid refinement levels. (Top) Precannula pressure. (Bottom) Postcannula pressure. The head-neck to descending aorta flow-split ratio is 40/60. Only one period of the experimental measurements is shown for clarity.

head-neck suction. Due to the low flow rate through the head-neck vessels, the inflow inertia needs to be attenuated before streaming to these vessels. This creates rotational flow (particles typically require three to four turns to exit the aorta) and a regional low velocity region inside of the flow domain. While the location of this region changes dynamically over the cardiac cycle, it is approximately located at the start of the DAo. Pressure field generated by the head-neck outlets interacts with the jet flow in a novel way and deflects its structure caudally, while this effect has been offset by the DAo flow once the cannula jet exits the arch region.

The most apparent characteristic of the CPB perfusion in the aortic arch is the presence of a high-speed jet that emerges from the 10 Fr tapered cannula tip. The jet eventually hits to the anterior wall of the descending aorta and bifurcates into the left subclavian and descending aorta. The cannula jet that splits into the left subclavian creates a recirculation zone at the entrance of this vessel. This flow structure is illustrated through the plotted path lines, Fig. 7(*b*), where particles are released from the inlet cannulla. The Reynolds and Womersley numbers during peak flow for this jet are calculated to be 1936 and 2, respectively, based on a 2.46 mm cannula diameter. Average Reynolds numbers are 1516 and 427 for the cannula inlet and descending aorta, respectively. Typical velocity fields are compared in Fig. 7(*c*).

During the cardiac cycle, the left subclavian artery is found to be perfused through swirling flow streams. Most importantly the innominate artery perfused through a tortuous pathway, which is assisted by the low pressure suction created by the exiting jet. Flow swirls (inner product of vorticity and velocity vector) in the outflow branches are calculated along the cardiac cycle, and average values are presented in Table 2 as an index of flow disturbance, recirculation, and high drag in these vessels. Nonphysiological flow swirl values are recorded at the left common carotid and subclavian arteries of the CPB model. Reduction of flow swirl in these vessels is also apparent from the particle flow pathways. This phenomenon is associated with the reduced flow energy as these two vessels receive blood flow deep from the DAo entrance and after following several complex swirls. The majority of the particles that end up at the anterior wall of the aortic arch also perfuse the head-neck vessels. Low velocity complex stagnant flow is observed in almost all parts of the pouch region of the aortic cross-clamp throughout the cardiac cycle, Figs. 7(*c*) and 8(*c*). Flow structures do not differ significantly between the 50/50 and 60/40 DAo/head-neck split cases; the latter features a larger percentage of particle pathlines going to the DAo and lesser cross-clamp pouch perfusion.

3.3 Flow Structures (Normal Pediatric Versus Normal Neonatal Aorta). The nondimensional numbers calculated for the normal pediatric (unscaled) 10 year old pediatric aorta and the neonatal aorta are summarized in Table 3. Pulsatile effects, based on ascending aorta diameter, are more important for pediatric flow compared with the neonatal aorta. At these physiological timepoints the velocity profiles during the acceleration and deceleration phases are plotted in Figs. 8(*a*) and 8(*b*) to demonstrate the changes in flow skewness with growth. During acceleration phase it is observed that flow skewness in the ascending aorta is along the posterior-posterior-right and posterior-posterior-left quadrants for the neonatal and age 10 original size aorta geometries, respectively. Further investigation on the neonatal aorta model (having 50/50 head-neck/DAo flow-split ratio) with a nonphysiological 40/60 head-neck/DAo flow-split ratio shows that skewness is also influenced by the flow-split, shifting it more toward the posterior-posterior-left quadrants (results not presented). Flow skewness at the descending aorta is along the anterior-right direction for all of the normal models studied.

During the peak and deceleration phases flow separation at the ascending aorta alters the flow profiles. At the ascending aorta maximum flow is observed through the anterior-right direction for both models. Descending aorta profiles are skewed toward the anterior-left direction.

Compared with the adult aortic flow simulations where head-neck to DAo flow-split is lower (15/85), the pediatric (40/60) and neonatal (50/50) flow-splits demonstrate increasingly more uniform velocity distribution in the aortic arch and the peak in the arch velocity profile also shifts toward the centerline.

3.4 Pulsatile Energy Cascade. Hemodynamic parameters that portray the pulsatile energy cascade in the aortic arch are tabulated in Table 4. SHE parameter represents the extra pulsatile energy that is delivered to each of the arterial vessels and influences the gross tissue perfusion. For the normal neonatal aorta the quality of pulsatile flow is considerably high and remains high at *all* arterial branches. On average, under normal physiological conditions, 60% and 13% of the inlet pulsatility are delivered to the head-neck vessels and descending aorta, respectively. In comparison, for the CPB configuration, only 9% of the inlet SHE is available at the left subclavian and DAo vessels. In the remaining head-neck vessels of the CPB model flow pulsatility is almost zero. Variations in the pulsatile branches of the head-neck vessels indicate that pulsatile energetics depend on geometry and cannula orientation, in addition to the pulsatile precanulla flow waveform.

Temporal changes in control volume power loss, Eq. (3), follow the inflow profile but slightly shifted due to pressure waveforms for both the CPB and neonatal Ao models. The peak and average power loss values are (310 mW, 43 mW) and (93 mW, 55 mW) for normal and CPB aorta models. Introduction of the cannula increases the average hydrodynamic power loss in the aortic junction by 28% compared with the normal aorta, in spite of the fact that cannula operates at a considerably lower average cardiac output (0.6 L/min versus 0.894 L/min). The spatial distribution of this quantity, the dissipation function, is suggested to be used as a performance parameter to improve the cannula tip design and its orientation. For the standard configuration, which is solely focused in this manuscript, the distribution of hydrodynamic dissipation is documented along several axial sections of the aortic arch, Fig. 9. It is observed that the shear layer due to the cannula jet extends well into the descending aorta contributing to the increase in power loss.

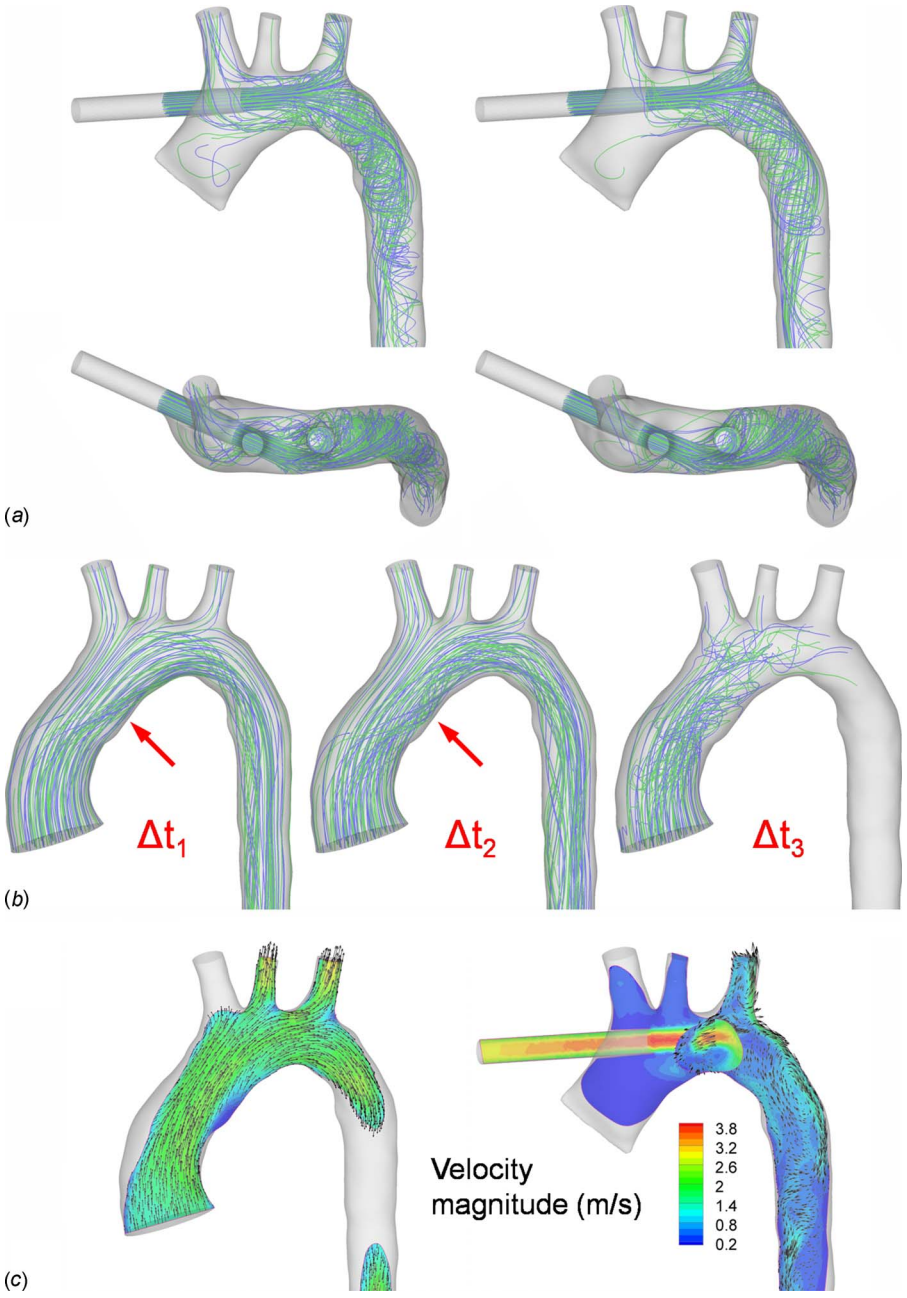

Fig. 7 (*a*) **Anterior and cranial views of the particle pathlines for the neonatal CPB model during acceleration (*t*=0–0.2 s, left) and second deceleration (*t*=0.3–0.525 s, right) phases. (*b*) Typical particle pathlines for the neonatal Ao observed during three instances; mid-, late deceleration, and end-systole, Δt_1, Δt_2, and Δt_3, respectively. The arrow indicates flow separation at the inferior wall of the arch. (*c*) Velocity magnitudes (m/s) during peak flow for normal neonatal Ao (left, *t*=0.05 s) and neonatal CPB assembly (right, *t*=0.2 s).**

3.5 Wall Shear Stress and Estimated Blood Damage. Equation (5) is integrated along the particle path lines to estimate the blood trauma for the physiological and for the CPB cannulation flow fields. Uniformly distributed particles ($n=30$) are released from the inlets at the end acceleration phase ($t=0.03$ s and $t=0.075$ s for neonatal and CPB models, respectively). Integration time gradually increased so that 95% of all the particles have left the solution domain for both models. Since the CPB model operates at a lower average cardiac output (0.6 L/min) compared with the neonatal model (0.894 L/min) the integration time is slightly larger for the former. Therefore the blood damage index reported here corresponds to the peak flow phase of both models. Calculated values are reported in Table 5 where CPB pathology caused a 288% increase in blood damage fraction compared with the physiological value.

Spatial and temporal cycle averaged values of WSS increased 55% over normal during CPB while WSS values calculated for both models can still be considered close to the adult physiological safe value of 10 N/m^2. Furthermore peak stress values are comparable for both models whereas the residence time and span of the peak shear stress in the CPB configuration were much higher compared with the physiological peak value. WSS hot-

Table 2 Average flow swirl over the cardiac cycle at the aortic branches for the normal neonatal model and CPB configuration. Flow swirl is normalized with dynamic pressure, $(\vec{\omega}\cdot\vec{V})/\rho V^2$. The head-neck/DAo flow-split ratio is 50/50 for both normal neonatal and cardiopulmonary bypass (CPB) configurations; ω and V are vorticity and velocity vectors, respectively. ρ is density of blood.

Swirl (m^2/kg)	Ascending aorta	Innominate artery	L. common carotid	Left subclavian	Descending aorta
Normal Ao	0.000	0.051	0.005	0.023	0.055
CPB Ao	0.000	0.005	43.625	4529.1	0.086

spots are observed at all the posterior-left walls of the head-neck vessels for the neonatal model (primary hot-spots) and only at the left subclavian for the CPB configuration (secondary hot-spot), Fig. 10. Wall shear stress for the CPB model is primarily associated with the squeezed cannula jet flow at the descending aorta inlet lumen (please see Fig. 10). Peak and average wall shear stress parameters are presented in Table 5 for both models.

4 Discussion

Surgical experience at the operating room indicates that even minor manual alterations of the CPB cannula orientation result in major changes in the cerebral blood flow of neonatal patients [74]. The local hemodynamic characterization of the standard neonatal CPB configuration highlights these three-dimensional geometrical determinants for achieving optimal fluid flow and tissue perfusion during CPB. The next objective of this study is to lay the foundation toward an integrated multiscale lumped circulation and local hemodynamics CPB model. While in this manuscript only two physiological flow-splits are studied, the complete hydrodynamic characteristic of the cannula/Ao assembly can be obtained by running batch CFD simulations at different flow-splits (including the variations in individual head-neck vessels). This information is valuable as it then can easily be plugged into a lumped-parameter model (as shown in Ref. [75] for another application) to provide

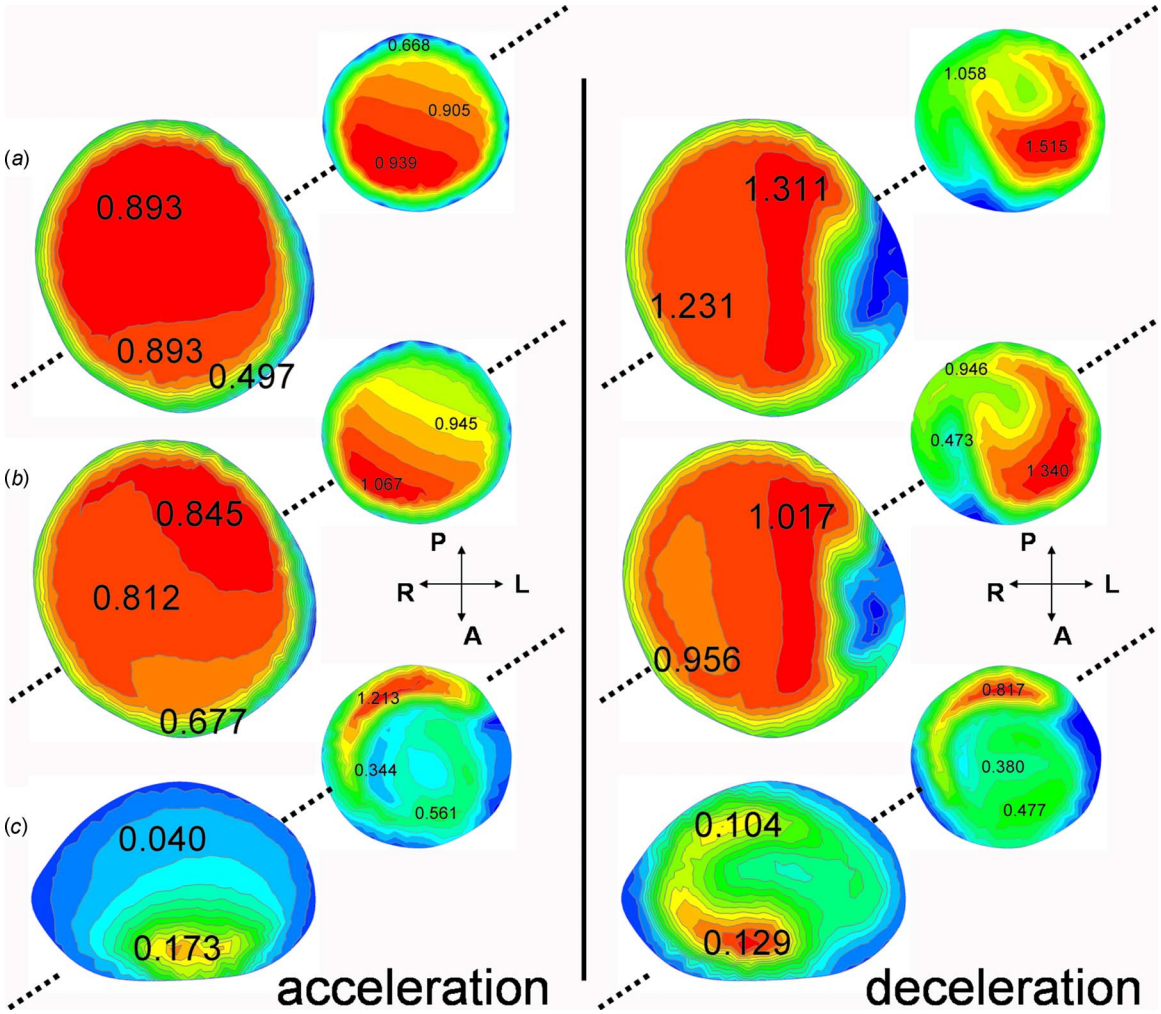

Fig. 8 Velocity magnitude (m/s) along the typical cross sections of the ascending and descending aortas during acceleration (left) and deceleration (right) phases for neonatal (*a*), pediatric (*b*), and cardiopulmonary bypass (*c*) models. The dashed line corresponds to the aortic arch centerline: (A) anterior, (P) posterior, (L) left, and (R) right directions.

Table 3 Nondimensional numbers governing fluid flow in the aorta models studied. The patient-specific aortic arch has two curvatures at the ascending aorta and the aortic arch with Dean numbers of 891 and 701, respectively. AAo: ascending aorta; DAo: descending aorta (*AAo Reynolds number for the CBP model is calculated based on the inlet cannula diameter); the head-neck/DAo flow-split ratio is 50/50 for both normal neonatal and cardiopulmonary bypass (CPB) configurations.

	Re (AAo) ave.	Re (AAo) peak	Re (DAo) ave.	Re (DAo) peak	Womersely
Neonatal	1128	6812	1538	9298	16.4
Pediatric	728	2984	822	3365	9.4
CPB*	1516	1936	422	546	2.0

the detailed cerebral perfusion. This approach is essential for pediatric applications as patients with congenital heart defects feature topologically complex circulatory networks that may also be hemodynamically unstable during particular surgical stages (first and second stage Fontan surgeries). Furthermore for 15% of the neonatal patients major branches of the Circle of Willis do not exist [76], while these patients are still being subjected to the standard perfusion strategies during CPB. An integrated lumped-parameter model will enable the global analysis and optimization of the perfusion strategy on a case-by-case basis, customized for each patient. It will also allow the evaluation of coronary perfusion during CPB.

Even though in this manuscript the CPB of a normal neonatal aorta morphology is studied, the presented patient-specific analysis approach is equally applicable to the abnormal congenital aortic arch anatomies. Most CPB strategies and protocols are very complex and physiologically demanding for the young patients. These risky CPB strategies once analyzed quantitatively could be deemed unnecessary for some patients, favoring a simpler CPB plan for them. For example, it can help perfusionists and surgeons to evaluate quantitatively whether a relatively simpler coarctation repair surgery can be undertaken without going through the complex perfusion strategies of the complete arch repair cases [77]. It will also help to evaluate whether cerebral perfusion is affected by patient's shunts or aorta pulmonary collaterals thereby complementing intraoperative imaging techniques [78]. In patients having dual vena cava [29] a decision whether to clamp both vena cava can be based on quantitative perfusion quality indices. The efficacy of retrograde emergency perfusion can also be evaluated for each patient prior to the surgery [79].

In this study both the calculated pre- and postcannula pressure waveforms matched the in vivo physiological measurements remarkably well: 7.4% mean difference for the postcannula. This degree of experimental agreement in such a complex problem is attributable to the meticulous physiological experimentation, the use of a recently available CFD model with specially selected numerical parameters, attention to the details of neonatal anatomy, and the virtual representation of the identical patient-specific neonatal CPB morphology. While it is acknowledged that a formal experimental validation on an actual aorta geometry is essential for conclusive model credibility, it should be noted that the same CFD model demonstrated excellent agreement with particle image velocimetry experiments for Re numbers up to 4000 in an unsteady complex cardiovascular benchmark test case conducted earlier [61]. In this manuscript an in vivo comparison is presented in a considerably complex vascular-device interaction problem. The only limitation of the model is the use of a rigid vessel wall model, which is partially justified in this study through the physiological waveforms as limited phase differences are observed between the inlet and outlet of the vessels for the region of interest, both experimentally and computationally.

Introduction of the cannula altered the normal hemodynamic conditions in the aortic arch that results in a severe pathological state for the patient that cannot be ignored even with the moderate less-demanding CPB waveform used in this study. Vascular trauma indices such as wall shear stress and hemolysis are considerably higher during CPB than under normal (55% and 288%, respectively) operating conditions. In this manuscript the CPB pathology is quantitatively presented and documented, which *urgently demands* improved designs, optimal cannula orientations, and waveforms to reduce the clinical consequences and improve the outcome of CPB surgery. For example, increased WSS region ($\sim$130 Pa at peak flow) due to the CPB jet colliding directly with the LSA and aortic isthmus periphery, Fig. 10, could possibly result in aortic dissection [78]; therefore, a slight cranial tilt of the cannula should be considered, which would also provide more energetic flow to the brain. Improved head-neck perfusion should be possible through further anterior inclination of the cannula tip. Our results also agree with the published clinical observation that for a standard CPB configuration, the most critical vessel for perfusion monitoring is the right common carotid artery [78]. Presented results will serve as a baseline for future design alternatives that can be quantitatively evaluated. This approach will also reduce the number of animal experiments required during the preliminary device design phase, for a typical device design which might well amount to several hundreds. To improve the local fluid dynamics of the CPB cannulation suggested designs can include different side-hole arrangements and variable internal cannula diameter profiles to control unsteady jet development. Furthermore ejector-pump effect of the high-speed cannula jet, which causes reduced flow (due to low vascular pressures as predicted in our study), or even "suction" from the innominate and left common carotid branches also deserves detailed parametric hydrodynamic investigation. The high swirling flow at the left common carotid and left subclavian should also be reduced as high swirl increases the wall drag almost five times, influencing the perfusion balance.

In a recent PC-MRI study, Fogel et al. have studied the in vivo hemodynamics and flow skewness of aortic flow profiles for both normal [80] and right [81] pediatric aortas ($n=13$ and $n=14$, re-

Table 4 Surplus hemodynamic energy (SHE) (ergs/cm^3) as a parameter of pulsatile waveform quality for the great vessels of the neonatal aortic arch. The head-neck/DAo flow-split ratio is 50/50 for both normal neonatal and cardiopulmonary bypass (CPB) configurations.

SHE (ergs/cm^3)	Ascending aorta	Innominate artery	L. common carotid	Left subclavian	Descending aorta
Neonatal	22,326	12,914	12,975	12,265	2835
CPB	7109	57	1	705	656

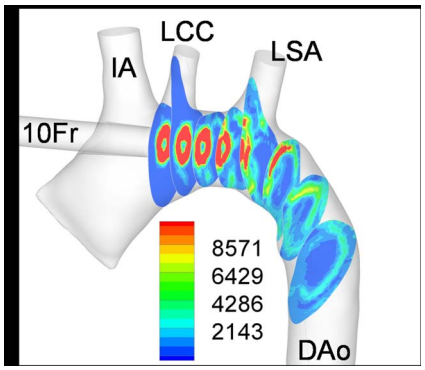

Fig. 9 The distribution of dissipation function (mW/m^3), Eq. (4), and the development of cannula jet shear layer for the CPB model at t=0.425 s. DAo: descending aorta, IA: innominate artery, LCC: left common carotid artery, and LSA: left subclavian artery.

spectively). While our study is limited to a single patient, similar flow structures are observed with detailed CFD velocity distributions. During late acceleration posterior-right received the greatest flow for the ascending aorta and the anterior descending flow rate is slightly higher than the posterior. During the peak acceleration and deceleration phase posterior flow dominates in the descending aorta and the left posterior flow is the lowest in the ascending aorta. This study also presented, to our knowledge, first time in literature the three-dimensional hemodynamics of a normal neonatal aortic arch. Combined with our recent study [44] and earlier biofluid dynamic studies of aortic arch, the hemodynamics of the human aorta can be quantified along the entire biological timeline and changes in mechanical loading can be correlated with large-scale vascular growth. Peak Reynolds numbers for the fetal, neonatal, pediatric, and adult aortas are 1063, 2984, 6812, and 4000–6000 [82,83], respectively. During fetal-to-neonatal transition the drastic increase in Reynolds number is associated with the closure of ductus arteriosus, and almost a double abrupt increase in the ascending aorta flow rate deserves further biophysical investigation (total cardiac output approximately remains constant for the late-gestation fetal and neonatal stages). The growth of the vessel diameter and the cardiac output change stabilizes during pediatric and adult stages.

Table 5 Wall shear stress (WSS) and index of hemolysis (10^6 D_{WG}), Eq. (5), for the aorta models studied. The head-neck/DAo flow-split ratio is 50/50 for both normal neonatal and cardiopulmonary bypass (CPB) configurations.

	WSS (peak) (N/m^2)	WSS (ave. peak) (N/m^2)	WSS (cycle ave.) (N/m^2)	MIH 10^6 D_{WG}
Neonatal	148	39	8.3	77
CPB	147	18	12.9	299

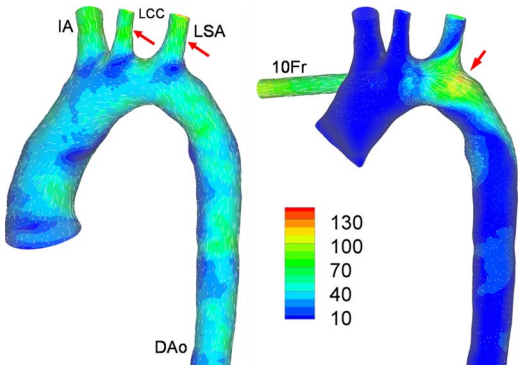

Fig. 10 Wall shear stress (N/m^2) and surface traction vectors plotted for normal and CPB aortas during peak flow. The arrows indicate the primary shear stress hot-spots for both models. For normal aorta high shear is observed at the head-neck vessels while squeezed stagnant CPB jet created high wall shear stress at the descending aorta entrance. DAo: descending aorta, IA: innominate artery, LCC: left common carotid artery, and LSA: left subclavian artery.

While it is well established that the Newtonian assumption is valid for large artery flows [84], non-Newtonian effects could still be critical for the empirical hemolysis model that is utilized in this study, Eq. (5). We like to highlight that this parameter is provided in order to "compare" normal versus the pathological neonatal aortic arch and to evaluate its significance in relation to the other hemodynamic performance parameters.

The major anatomical dimensions of both models are validated rigorously with the existing clinical measurements (see Sec. 2.1). Whereas for the complete 3D morphological information on detailed but arguably secondary geometrical variations of the normal aorta topology such as taper, the radius of curvature does not exist in literature, to our best knowledge, including the pediatric/neonatal patients (even for the adult aortic arch, see Ref. [85]). Especially reaching a statistical conclusion on these secondary anatomical features requires risky sedated scans of a large number of normal subjects. In addition, according to the information we have from the normal adult aortic arch, subject-to-subject variation in the great vessels is considerable, for example, at age 20 the aortic root radius varies from 2 cm to 3 cm (±20%) [85]. In addition, considerable variations in the dynamic motion patterns and normal head-neck vessel branch configurations exist [86]; 21% of normal individuals have a common origin of the brachiocephalic trunk and the left common carotid artery [87]. Most importantly, these secondary variations will be relatively minor compared with the subject-to-subject variations of the *diseased* aortic morphologies that are usually encountered during CPB as the main purpose of these surgeries is to palliate congenital cardiac defects. Therefore given all these complex 3D variations our approach that introduces the patient-specific aspect to this study is reasonable.

Among the 170 patients that have 3D MRI anatomical/flow information in our database, only two are scanned at 6 months of age. We have 15 patients less than age 2 and 35 patients at age between 2 and 3 years old. Unfortunately neither of these patients has the normal aortic arch anatomy. The youngest patient that could be used in this study with a normal arch is of age 3 years old but this patient has a mirror image right-sided aortic arch topology. We identified only three patients with normal aortic arches with 10, 8, and 19 years old. The 8 years old patient is excluded as she had an unusually small aortic root diameter for the age range (3.2 mm). Therefore the 10 year old patient is selected and the anatomical validity of this selection is confirmed through individual discussions with three experienced pediatric cardiologists and two pediatric surgeons. In spite of the aforementioned scarcity of the pediatric/neonatal anatomical data for research purposes, it is absolutely possible to acquire presurgical patient-specific cardiovascular data from the neonatal patients as long as there is a valid clinical justification. Such clinical scans are routinely performed in clinical practice for diagnosis and presurgical catheterization conferences. Our manuscript illustrates how such patient-specific 3D data could provide additional physiological understanding. Finally, the justification of using a rigid model in this study, as opposed to a compliant wall model to estimate the pulsatile energy losses, is founded on the following. (1) Has acceptably well agreement with the in vivo measurements performed on an established neonatal CPB animal model. (2) As in most arterial hemodynamic applications, for aortic flows the use of compliant models alone does not bring much improvement

on the accuracy of the results over simpler and computationally more efficient rigid models [39,40,48,88–90]. The vessel diameter change over the cardiac cycle is around ~11% for the neonatal pediatric stages, similar to the healthy adult human aortic arch [91–93]. (3) The present study particularly focuses on the *comparative* differences of physiological and pathological CPB states. (4) The major energy loss in the arterial system is due to the *hydrodynamic* dissipation. The "pulsatile energy dissipated" at the vessel wall over the cardiac cycle is essentially zero as large arterial vessels are reasonably *elastic* demonstrating negligible hysteresis [94,95]. Viscoelastic behavior of the vessel wall becomes prominent in smaller arteries [96]. (5) Full fluid structure interaction (FSI) analysis is still very challenging for surgical planning applications, which demand almost real-time CFD results. Particular challenges are unknown and spatially varying vessel material properties.

The computational fluid dynamics model enables us to calculate the *distribution* of the pulsatile energy to each of the aortic arch vessels. This information could be quite difficult to obtain through animal experiments or in vitro benchtop models. The present study further demonstrates that the geometry and location of the CPB cannula are critical for reduced blood damage, improved pulsatility, and balanced perfusion. Drastic differences between the normal and CPB hemodynamic conditions further indicate that there is still room for improvement. A validated CFD model is a valuable tool toward this objective, which will allow the analysis of different CPB designs efficiently and will lead to an optimal neonatal CPB configuration.

5 Conclusion

A generic, experimentally validated, second-order accurate CFD model of the patient-specific CPB model is developed. The physiological neonatal aortic flow is compared in detail with the pathologic state of CPB cannulation. Hemodynamic conditions have changed drastically with the introduction of cannula, which can be summarized as follows.

- Disturbed flow structures are observed during CPB even with a moderate and safe freestream cannulla jet inlet waveform.
- Pulsatile hemodynamic energy of the CPB configuration is limited to the left subclavian and descending aorta and only ~9% of the inflow pulsatility left to support brain tissue perfusion. In the normal neonatal arch ~60% of the inlet pulsatile hemodynamic energy, distributed equally, is delivered to the brain.
- While the peak WSS magnitudes are similar for both models, differences in the residence times caused an almost double increase in the temporally and spatially averaged wall shear stress values during a moderate CPB operation.
- Relative hemolysis index increased 288%, which demands extra biomedical engineering design emphasis compared with the WSS improvement.
- Power loss increased to 28%.
- Local hemodynamic performance strongly depends on the cannulation geometry. Improperly oriented cannulas can influence perfusion and generate reduced pressure and suction backflow at the right head-neck vessels.

In this manuscript the baseline hemodynamic state of a typical relatively safe CPB cannulation is presented. Major differences in perfusion quality, blood damage, and WSS loading demand improved the CPB cannulation and better bioengineering designs. With this generic validated neonatal CPB model, optimal CPB configurations, waveforms, and tip designs can be evaluated prior to (or in place of) the preliminary animal experiments. Complex perfusion strategies could also be analyzed once integrated with a lumped-parameter model to help the surgical decision making process.

Acknowledgment

This work utilized the National Heart, Lung, and Blood Institute Fontan anatomy database through Grant No. HL67622. We also acknowledge Steven Marzec (Gatech) for his technical assistance in high-performance parallel CFD runs and Pittsburgh Supercomputing Center Grant No. CCR080013.

References

[1] Ungerleider, R. M., 2005, "Practice Patterns in Neonatal Cardiopulmonary Bypass," ASAIO J., **51**(6), pp. 813–815.
[2] Papantchev, V., Hristov, S., Todorova, D., Naydenov, E., Paloff, A., Nikolov, D., and Tschirkov, A. O. W., 2007, "Some Variations of the Circle of Willis, Important for Cerebral Protection in Aortic Surgery—A Study in Eastern Europeans," Eur. J. Cardiothorac Surg., **31**(6), pp. 982–989.
[3] Schumacher, J., Eichler, W., Heringlake, M., Sievers, H. H., and Klotz, K. F., 2004, "Intercompartmental Fluid Volume Shifts During Cardiopulmonary Bypass Measured by A-Mode Ultrasonography," Perfusion, **19**(5), pp. 277–281.
[4] Ündar, A., Vaughn, W. K., and Calhoon, J. H., 2000, "The Effects of Cardiopulmonary Bypass and Deep Hypothermic Circulatory Arrest on Blood Viscoelasticity and Cerebral Blood Flow in a Neonatal Piglet Model," Perfusion, **15**(2), pp. 121–128.
[5] Ündar, A., Koenig, K. M., Frazier, O. H., and Fraser, C. D., 2000, "Impact of Membrane Oxygenators on Pulsatile Versus Nonpulsatile Perfusion in a Neonatal Model," Perfusion, **15**, pp. 111–120.
[6] Travis, A. R., Giridharan, G. R., Pantalos, G. M., Dowling, R. D., Prabhu, S. D., Slaughter, M. S., Sobieski, M., Undar, A., Farrar, D. J., and Koenig, S. C., 2007, "Vascular Pulsatility in Patients With a Pulsatile- or Continuous-Flow Ventricular Assist Device," J. Thorac. Cardiovasc. Surg., **133**(2), pp. 517–523.
[7] Hetzer, R., Loebe, M., Potapov, E. V., Weng, Y., Stiller, B., Hennig, E., Alexi-Meskishvili, V., and Lange, P. E., 1998, "Circulatory Support With Pneumatic Paracorporeal Ventricular Assist Device in Infants and Children," Ann. Thorac. Surg., **66**, pp. 1498–1506.
[8] Konertz, W., Hotz, H., Schneider, M., Redlin, M., and Reul, H., 1997, "Clinical Experience With the MEDOS HIA-VAD System in Infants and Children: A Preliminary Report," Ann. Thorac. Surg., **63**, pp. 1138–1144.
[9] Skinner, S. C., Hirschl, R. B., and Bartlett, R. H., 2006, "Extracorporeal Life Support," Semin Pediatr. Surg., **15**(4), pp. 242–250.
[10] Hetzer, R., Potapov, E. V., Stiller, B., Weng, Y., Hübler, M., Lemmer, J., Alexi-Meskishvili, V., Redlin, M., Merkle, F., Kaufmann, F., and Hennig, E., 2006, "Improvement in Survival After Mechanical Circulatory Support With Pneumatic Pulsatile Ventricular Assist Devices in Pediatric Patients," Ann. Thorac. Surg., **82**, pp. 917–925.
[11] Ündar, A., 2002, "The ABCs of Research on Pulsatile Versus Nonpulsatile Perfusion During Cardiopulmonary Bypass," Med. Sci. Monit., **8**(12), pp. ED21–4.
[12] Undar, A., Masai, T., Beyer, E. A., Goddard-Finegold, J., McGarry, M. C., and Fraser, C. D., 2002, "Pediatric Physiologic Pulsatile Pump Enhances Cerebral and Renal Blood Flow During and After Cardiopulmonary Bypass," Artif. Organs, **26**(11), pp. 919–923.
[13] Mavroudis, C., 1978, "To Pulse or not to Pulse," Ann. Thorac. Surg., **25**(3), pp. 259–271.
[14] Ji, B., and Undar, A., 2007, "Precise Quantification of Pressure-Flow Waveforms During Pulsatile and Nonpulsatile Perfusion," J. Thorac. Cardiovasc. Surg., **133**(5), p. 1395.
[15] Weiss, W. J., Lukic, B., and Ündar, A., 2005, "Energy Equivalent Pressure and Total Hemodynamic Energy Associated With the Pressure-Flow Waveforms of a Pediatric Pulsatile Ventricular Assist Device," ASAIO J., **51**(5), pp. 614–617.
[16] Ündar, A., Owens, R. W., McGarry, M. C., Surprise, D. L., Kilpack, V. D., Mueller, M. W., McKenzie, E. D., and Fraser, C. D., 2005, "Comparison of Hollow-Fiber Membrane Oxygenators in Terms of Pressure Drop of the Membranes During Normothermic and Hypothermic Cardiopulmonary Bypass in Neonates," Perfusion, **20**, pp. 135–138.
[17] Ündar, A., Lodge, A. J., Daggett, C. W., Runge, T. M., Ungerleider, R. M., and Calhoon, J. H., 1998, "The Type of Aortic Cannula and Membrane Oxygenator Affect the Pulsatile Waveform Morphology Produced by a Neonate-Infant Cardiopulmonary Bypass System In Vivo," Artif. Organs, **22**(8), pp. 681–686.
[18] Gu, Y. J., De Kroon, T. L., Elstrodt, J. M., van Oeveren, W., Boonstra, P. W., and Rakhorst, G., 2005, "Augmentation of Abdominal Organ Perfusion During Cardiopulmonary Bypass With a Novel Intra-Aortic Pulsatile Catheter Pump," Int. J. Artif. Organs, **28**(1), pp. 35–43.
[19] Kaps, M., Haase, A., Mulch, J., Stertmann, W. A., and Thiel, A., 1989, "Pulsatile Flow Pattern in Cerebral Arteries During Cardiopulmonary Bypass. An Evaluation Based on Transcranial Doppler Ultrasound," J. Cardiovasc. Surg., **30**(1), pp. 16–19.
[20] Harrington, D. K., Fragomeni, F., and Bonser, R. S., 2007, "Cerebral Perfusion," Ann. Thorac. Surg., **83**(2), pp. S799–804.
[21] Ündar, A., Masai, T., Yang, S., Goddard-Finegold, J., Frazier, O. H., and Fraser, C. D., 1999, "Effects of Perfusion Mode on Regional and Global Organ Blood Flow in a Neonatal Piglet Model," Ann. Thorac. Surg., **68**, pp. 1336–1343.
[22] May-Newman, K. D., Hillen, B. K., Sironda, C. S., and Dembitsky, W., 2004, "Effect of LVAD Outflow Conduit Insertion Angle on Flow Through the Na-

tive Aorta," J. Med. Eng. Technol., **28**(3), pp. 105–109.
[23] May-Newman, K., Hillen, B., and Dembitsky, W., 2006, "Effect of Left Ventricular Assist Device Outflow Conduit Anastomosis Location on Flow Patterns in the Native Aorta," ASAIO J., **52**(2), pp. 132–139.
[24] Torii, R., Wood, N. B., Hughes, A. D., Thom, S. A., Aguado-Sierra, J., Davies, J. E., Francis, D. P., Parker, K. H., and Xu, X. Y., 2007, "A Computational Study on the Influence of Catheter-Delivered Intravascular Probes on Blood Flow in a Coronary Artery Model," J. Biomech., **40**(11), pp. 2501–2509.
[25] Park, J. Y., Park, C. Y., and Min, B. G., 2007, "A Numerical Study on the Effect of Side Hole Number and Arrangement in Venous Cannulae," J. Biomech., **40**(5), pp. 1153–1157.
[26] Andersen, M. N., Ringgaard, S., Hasenkam, J. M., and Nygaard, H., 2004, "Quantitative Hemodynamic Evaluation of Aortic Cannulas," Perfusion, **19**(5), pp. 323–330.
[27] Foust, J., and Rockwell, D., 2006, "Structure of the Jet From a Generic Catheter Tip," Exp. Fluids, **41**, pp. 543–558.
[28] Pekkan, K., Kitajima, H., Forbess, J., Fogel, M., Kanter, K., Parks, J. M., Sharma, S., and Yoganathan, A. P., 2005, "Total Cavopulmonary Connection Flow With Functional Left Pulmonary Artery Stenosis—Fenestration and Angioplasty In Vitro," Circulation, **112**(21), pp. 3264–3271.
[29] de Zélicourt, D., Pekkan, K., Parks, W. J., Kanter, K., Fogel, M., and Yoganathan, A. P., 2006, "Flow Study of an Extra-Cardiac Connection With Persistent Left Superior Vena Cava," J. Thorac. Cardiovasc. Surg., **131**(4), pp. 785–791.
[30] Pekkan, K., Whited, B., Kanter, K., Sharma, S., de Zélicourt, D., Sundareswaran, K., Frakes, D., Rossignac, J., and Yoganathan, A. P., 2008, "Patient Specific Surgical Planning and Hemodynamic Computational Fluid Dynamics Optimization Through Free-Form Haptic Anatomy Editing Tool (SURGEM)," Med. Biol. Eng. Comput., to be published.
[31] Caro, C. G., Pedley, T. J., Schroter, R. C., and Seed, W. A., 1978, *The Mechanics of the Circulation*, Oxford University Press, Oxford.
[32] McDonald, D. A., 1974, *Blood Flow in Arteries*, Edwards, Ann Arbor, MI/Arnold, London.
[33] Fung, Y. C., 1984, *Biodynamics: Circulation*, Springer, New York.
[34] Mori, D., and Yamaguchi, T., 2002, "Computational Fluid Dynamics Modeling and Analysis of the Effect of 3-D Distortion of the Human Aortic Arch," Comput. Methods Biomech. Biomed. Eng., **5**(3), pp. 249–260.
[35] Nakamura, M., Wada, S., and Yamaguchi, T., 2006, "Computational Analysis of Blood Flow in an Integrated Model of the Left Ventricle and the Aorta," J. Biomech. Eng., **128**, pp. 837–843.
[36] Morris, L., Delassus, P., Callanan, A., Walsh, M., Wallis, F., Grace, P., and McGloughlin, T., 2005, "3-D Numerical Simulation of Blood Flow Through Models of the Human Aorta," J. Biomech. Eng., **127**, pp. 767–775.
[37] Wood, N. B., Weston, S. J., Kilner, P. J., Gosman, A. D., and Firmin, D. N., 2001, "Combined MR Imaging and CFD Simulation of Flow in the Human Descending Aorta," J. Magn. Reson Imaging, **13**(5), pp. 699–713.
[38] Leuprecht, A., Kozerke, S., Boesiger, P., and Perktold, K., 2003, "Blood Flow in the Human Ascending Aorta: A Combined MRI and CFD Study," J. Eng. Math., **47**, pp. 387–404.
[39] Jin, S., Oshinski, J., and Giddens, D. P., 2003, "Effects of Wall Motion and Compliance on Flow Patterns in the Ascending Aorta," J. Biomech. Eng., **125**(3), pp. 347–354.
[40] Suo, J., 2005, "Investigation of Blood Flow Patterns and Hemodynamics in the Human Ascending Aorta and Major Trunks of Right and Left Coronary Arteries Using Magnetic Resonance Imaging and Computational Fluid Dynamics," Georgia Institute of Technology, Atlanta, GA.
[41] Shahcheraghi, N., Dwyer, H. A., Cheer, A. Y., Barakat, A. I., and Rutaganira, T., 2002, "Unsteady and Three-Dimensional Simulation of Blood Flow in the Human Aortic Arch," J. Biomech. Eng., **124**(4), pp. 378–387.
[42] Feintuch, A., Ruengsakulrach, P., Lin, A., Zhang, J., Zhou, Y. Q., Bishop, J., Davidson, L., Courtman, D., Foster, F. S., Steinman, D. A., Henkelman, R. M., and Ethier, C. R., 2006, "Hemodynamics in the Mouse Aortic Arch as Assessed by MRI, Ultrasound, and Numerical Modeling," Am. J. Physiol. Heart Circ. Physiol., **292**(2), pp. H884–892.
[43] Jin, S., Ferrara, D. E., Sorescu, D., Guldberg, R. E., Taylor, W. R., and Giddens, D. P., 2007, "Hemodynamic Shear Stresses in Mouse Aortas: Implications for Atherogenesis," Arterioscler., Thromb., Vasc. Biol., **27**(2), pp. 346–351.
[44] Pekkan, K., Dasi, L. P., Nourparvar, P., Yerneni, S., Tobita, K., Fogel, M. A., Keller, B., and Yoganathan, A., 2008, "In Vitro Hemodynamic Investigation of the Embryonic Aortic Arch at Late Gestation," J. Biomech., **41**(8), pp. 1697–1706.
[45] Deplano, V., Knapp, Y., Bertrand, E., and Gaillard, E., 2007, "Flow Behaviour in an Asymmetric Compliant Experimental Model for Abdominal Aortic Aneurysm," J. Biomech., **40**(11), pp. 2406–2413.
[46] Di Martino, E. S., Guadagni, G., Fumero, A., Ballerini, G., Spirito, R., Biglioli, P., and Redaelli, A., 2001, "Fluid-Structure Interaction Within Realistic Three-Dimensional Models of the Aneurysmatic Aorta as a Guidance to Assess the Risk of Rupture of the Aneurysm," Med. Eng. Phys., **23**(9), pp. 647–655.
[47] Kleinstreuer, C., Li, Z., and Farber, M. A., 2007, "Fluid-Structure Interaction Analyses of Stented Abdominal Aortic Aneurysms," Annu. Rev. Biomed. Eng., **9**, pp. 169–204.
[48] Papaharilaou, Y., Ekaterinaris, J. A., Manousaki, E., and Katsamouris, A. N., 2007, "A Decoupled Fluid Structure Approach for Estimating Wall Stress in Abdominal Aortic Aneurysms," J. Biomech., **40**(2), pp. 367–377.
[49] Valencia, A. A., Guzman, A. M., Finol, E. A., and Amon, C. H., 2006, "Blood Flow Dynamics in Saccular Aneurysm Models of the Basilar Artery," ASME J. Biomech. Eng., **128**(4), pp. 516–526.
[50] Ettinger, S. J., 1975, *Textbook of Veterinary Internal Medicine*, Saunders, Philadelphia, PA.
[51] Capps, S. B., Elkins, R. C., and Fronk, D. M., 2000, "Body Surface Area as a Predictor of Aortic and Pulmonary Valve Diameter," J. Thorac. Cardiovasc. Surg., **119**(5), pp. 975–982.
[52] Fitzgerald, S. W., Donaldson, J. S., and Poznanski, A. K., 1987, "Pediatric Thoracic Aorta: Normal Measurements Determined With CT," Radiology, **165**(3), pp. 667–669.
[53] Tan, J., Silverman, N. H., Hoffman, J. I., Villegas, M., and Schmidt, K. G., 1992, "Cardiac Dimensions Determined by Cross-Sectional Echocardiography in the Normal Human Fetus From 18 Weeks to Term," Am. J. Cardiol., **70**(18), pp. 1459–1467.
[54] Poutanen, T., Tikanoja, T., Sairanen, H., and Jokinen, E., 2003, "Normal Aortic Dimensions and Flow in 168 Children and Young Adults," Clin. Physiol. Funct. Imaging, **23**(4), pp. 224–229.
[55] Frakes, D. H., Conrad, C. P., Healy, T. M., Monaco, J. W., Fogel, M., Sharma, S., Smith, M. J., and Yoganathan, A. P., 2003, "Application of an Adaptive Control Grid Interpolation Technique to Morphological Vascular Reconstruction," IEEE Trans. Biomed. Eng., **50**(2), pp. 197–206.
[56] Pekkan, K., Zelicourt, D., Ge, L., Sotiropoulos, F., Frakes, D., Fogel, M., and Yoganathan, A., 2005, "Physics-Driven CFD Modeling of Complex Anatomical Cardiovascular Flows—A TCPC Case Study," Ann. Biomed. Eng., **33**(3), pp. 284–300.
[57] Whitehead, K. K., Pekkan, K., Kitajima, H. D., Paridon, S. M., Yoganathan, A.P., and Fogel, M. A., 2007 "Non-Linear Power Loss During Exercise in Single-Ventricle Patients After the Fontan: Insights From Computational Fluid Dynamics," Circulation, **116**, pp. I-165–I-171
[58] Frakes, D. H., Smith, M. J., Parks, J., Sharma, S., Fogel, S. M., and Yoganathan, A. P., 2005, "New Techniques for the Reconstruction of Complex Vascular Anatomies From MRI Images," J. Cardiovasc. Magn. Reson., **7**(2), pp. 425–432.
[59] Chen, H. Y., Einstein, D. R., Chen, K., and Vesely, I., 2005, "Computational Modeling of Vascular Clamping: A Step Toward Simulating Surgery," *Proceedings of the 2005 IEEE Engineering in Medicine and Biology 27th Annual Conference*, Shanghai, China, Sep. 1–4.
[60] Rossignac, J., Pekkan, K., Whited, B., Kanter, K., Sharma, S., and Yoganathan, A., 2006, "Surgem: Next Generation CAD Tools for Interactive Patient-Specific Surgical Planning and Hemodynamic Analysis," Georgia Institute of Technology, Atlanta, GA.
[61] Wang, C., Pekkan, K., de Zélicourt, D., Horner, M., Parihar, A., Kulkarni, A., and Yoganathan, A. P., 2007, "Progress in the CFD Modeling of Flow Instability in Anatomical Total Cavopulmonary Connections," Ann. Biomed. Eng., **35**(11), pp. 1840–1856.
[62] Salim, M. A., DiSessa, T. G., Arheart, K. L., and Alpert, B. S., 1995, "Contribution of Superior Vena Caval Flow to Total Cardiac Output in Children. A Doppler Echocardiographic Study," Circulation, **92**(7), pp. 1860–1865.
[63] Fischer, P. F., Loth, F., Lee, S. E., Lee, S., Smith, D. S., and Bassiouny, H. S., 2007, "Simulation of High-Reynolds Number Vascular Flows," Comput. Methods Biomech. Biomed. Eng., **196**, pp. 3049–3060.
[64] Fogel, M. A., Weinberg, P. M., Rychik, J., Hubbard, A., Jacobs, M., Spray, T. L., and Haselgrove, J., 1999, "Caval Contribution to Flow in the Branch Pulmonary Arteries of Fontan Patients With a Novel Application of Magnetic Resonance Presaturation Pulse," Circulation, **99**(9), pp. 1215–1221.
[65] Undar, A., Masai, T., Yang, S. Q., Eichstaedt, H. C., McGarry, M. C., Vaughn, W. K., Goddard-Finegold, J., and Fraser, C. D., Jr., 2001, "Global and Regional Cerebral Blood Flow in Neonatal Piglets Undergoing Pulsatile Cardiopulmonary Bypass With Continuous Perfusion at 25 Degrees C and Circulatory Arrest at 18 Degrees C," Perfusion, **16**(6), pp. 503–510.
[66] Undar, A., 2003, "Universal and Precise Quantification of Pulsatile and Nonpulsatile Pressure Flow Waveforms is Necessary for Direct and Adequate Comparisons Among the Results of Different Investigators," Perfusion, **18**(2), pp. 135–136.
[67] Healy, T. M., Lucas, C., and Yoganathan, A. P., 2001, "Noninvasive Fluid Dynamic Power Loss Assessments for Total Cavopulmonary Connections Using the Viscous Dissipation Function: A Feasibility Study," ASME J. Biomech. Eng., **123**(4), pp. 317–324.
[68] Venkatachari, A. K., Halliburton, S. S., Setser, R. M., White, R. D., and Chatzimavroudis, G. P., 2007, "Noninvasive Quantification of Fluid Mechanical Energy Losses in the Total Cavopulmonary Connection With Magnetic Resonance Phase Velocity Mapping," Magn. Reson. Imaging, **25**(1), pp. 101–109.
[69] Giersiepen, M., Wurzinger, L. J., Opitz, R., and Reul, H., 1990, "Estimation of Shear Stress-Related Blood Damage in Heart Valve Prostheses-In Vitro Comparison of 25 Aortic Valves," Int. J. Artif. Organs, **13**(5), pp. 300–306.
[70] Farinas, M. I., Garon, A., Lacasse, D., and N'Dri, D., 2006, "Asymptotically Consistent Numerical Approximation of Hemolysis," ASME J. Biomech. Eng., **128**(5), pp. 688–696.
[71] Garon, A., and Farinas, M. I., 2004, "Fast Three-Dimensional Numerical Hemolysis Approximation," Artif. Organs, **28**(11), pp. 1016–1025.
[72] Arora, D., Behr, M., and Pasquali, M., 2004, "A Tensor-Based Measure for Estimating Blood Damage," Artif. Organs, **28**(11), pp. 1002–1015.
[73] Arvand, A., Hormes, M., and Reul, H., 2005, "A Validated Computational Fluid Dynamics Model to Estimate Hemolysis in a Rotary Blood Pump," Artif. Organs, **29**(7), pp. 531–540.
[74] Austin, E. H., 2007, "Neuromonitoring During Pediatric Cardiopulmonary Bypass," *Proceedings of the Third International Conference on Pediatric Me-*

chanical Circulatory Support Systems and Pediatric Cardiopulmonary Perfusion, Heshey, PA, May 17–19.
[75] Pekkan, K., Frakes, D., De Zelicourt, D., Lucas, C. W., Parks, W. J., and Yoganathan, A. P., 2005, "Coupling Pediatric Ventricle Assist Devices to the Fontan Circulation: Simulations With a Lumped-Parameter Model," ASAIO J., **51**(5), pp. 618–628.
[76] Moore, S., David, T., Chase, J. G., Arnold, J., and Fink, J., 2006, "3D Models of Blood Flow in the Cerebral Vasculature," J. Biomech., **39**(8), pp. 1454–1463.
[77] Bakhtiary, F., Dogan, S., Risteski, P., Ackermann, H., Oezaslan, F., Kleine, P., Moritz, A., and Aybek, T., 2007, "Mild Hypothermic (30C) Body Perfusion During Replacement of the Aortic Arch With a Novel Arterial Perfusion Cannula," J. Thorac. Cardiovasc. Surg., **133**(6), pp. 1637–1639.
[78] Orihashi, K., Matsuura, Y., Sueda, T., Watari, M., Okada, K., Sugawara, Y., and Ishii, O., 2000, "Aortic Arch Branches Are no Longer a Blind Zone for Transesophageal Echocardiography: A New Eye for Aortic Surgeons," J. Thorac. Cardiovasc. Surg., **120**(3), pp. 466–472.
[79] Yeh, T., Jr., Austin, E. H., III, Sehic, A., and Edmonds, H. L., Jr., 2003, "Rapid Recognition and Treatment of Cerebral Air Embolism: The Role of Neuromonitoring," J. Thorac. Cardiovasc. Surg., **126**(2), pp. 589–591.
[80] Fogel, M. A., Weinberg, P. M., and Haselgrove, J., 2002, "Nonuniform Flow Dynamics in the Aorta of Normal Children: A Simplified Approach to Measurement Using Magnetic Resonance Velocity Mapping," J. Magn. Reson Imaging, **15**(6), pp. 672–678.
[81] Fogel, M. A., Weinberg, P. M., and Haselgrove, J., 2003, "Flow Volume Asymmetry in the Right Aortic Arch in Children With Magnetic Resonance Phase Encoded Velocity Mapping," Am. Heart J., **145**(1), pp. 154–161.
[82] Stein, P. D., and Sabbah, H. N., 1976, "Turbulent Blood Flow in the Ascending Aorta of Humans With Normal and Diseased Aortic Valves," Circ. Res., **39**(1), pp. 58–65.
[83] Ku, D. N., 1997, "Blood Flow in Arteries," Annu. Rev. Fluid Mech., **29**, pp. 399–434.
[84] Lee, S. W., and Steinman, D. A., 2007, "On the Relative Importance of Rheology for Image-Based CFD Models of the Carotid Bifurcation," ASME J. Biomech. Eng., **129**(2), pp. 273–278.
[85] Hager, A., Kaemmerer, H., Rapp-Bernhardt, U., Blucher, S., Rapp, K., Bernhardt, T. M., Galanski, M., and Hess, J., 2002, "Diameters of the Thoracic Aorta Throughout Life as Measured With Helical Computed Tomography," J. Thorac. Cardiovasc. Surg., **123**(6), pp. 1060–1066.
[86] Osborn, A., 1999, *Diagnostic Cerebral Angiography*, Lippincott, Philadelphia, PA/Williams & Wilkins, Baltimore, MD.
[87] Szpinda, M., 2007, "Morphometric Study of the Brachiobicarotid Trunk in Human Fetuses," Ann. Anat. Pathol. (Paris), **189**(6), pp. 569–574.
[88] Leuprecht, A., Perktold, K., Prosi, M., Berk, T., Trubel, W., and Schima, H., 2002, "Numerical Study of Hemodynamics and Wall Mechanics in Distal End-to-Side Anastomoses of Bypass Grafts," J. Biomech., **35**(2), pp. 225–236.
[89] Moayeri, M. S., and Zendehbudi, G. R., 2003, "Effects of Elastic Property of the Wall on Flow Characteristics Through Arterial Stenoses," J. Biomech., **36**(4), pp. 525–535.
[90] Perktold, K., and Rappitsch, G., 1995, "Computer Simulation of Local Blood Flow and Vessel Mechanics in a Compliant Carotid Artery Bifurcation Model," J. Biomech., **28**(7), pp. 845–856.
[91] Cartier, M. S., Davidoff, A., Warneke, L. A., Hirsh, M. P., Bannon, S., Sutton, M. S., and Doubilet, P. M., 1987, "The Normal Diameter of the Fetal Aorta and Pulmonary Artery: Echocardiographic Evaluation in Utero," AJR, Am. J. Roentgenol., **149**(5), pp. 1003–1007.
[92] Struijk, P. C., Wladimiroff, J. W., Hop, W. C., and Simonazzi, E., 1992, "Pulse Pressure Assessment in the Human Fetal Descending Aorta," Ultrasound Med. Biol., **18**(1), pp. 39–43.
[93] Studinger, P., Lenard, Z., Reneman, R., and Kollai, M., 2000, "Measurement of Aortic Arch Distension Wave With the Echo-Track Technique," Ultrasound Med. Biol., **26**(8), pp. 1285–1291.
[94] Stylianopoulos, T., and Barocas, V. H., 2007, "Multiscale, Structure-Based Modeling for the Elastic Mechanical Behavior of Arterial Walls," ASME J. Biomech. Eng., **129**(4), pp. 611–618.
[95] Zhao, S., Xu, X., and Collins, M., 1998, "The Numerical Analysis of Fluid-Solid Interactions for Blood Flow in Arterial Structures Part 1: A Review of Models for Arterial Wall Behavior," Proc. Inst. Mech. Eng., Part H: J. Eng. Med., **212**, pp. 229–240.
[96] Bessems, D., Giannopapa, C. G., Rutten, M. C., and van de Vosse, F. N., 2008, "Experimental Validation of a Time-Domain-Based Wave Propagation Model of Blood Flow in Viscoelastic Vessels," J. Biomech., **41**(2), pp. 284–291.